

Revisiting the Magnetic Field of the L183 Starless Core

JANIK KAROLY,^{1,2} ARCHANA SOAM,² B-G ANDERSSON,² SIMON COUDÉ,² PIERRE BASTIEN,³ JOHN E. VAILLANCOURT,⁴ AND
CHANG WON LEE^{5,6}

¹*Department of Physics, Santa Clara University, Santa Clara, 500 El Camino Real, Santa Clara, CA, USA*

²*SOFIA Science Center, Universities Space Research Association, NASA Ames Research Center, M.S. N232-12, Moffett Field, CA 94035, USA*

³*Institut de Recherche sur les Exoplanètes (iREx) & Centre de Recherche en Astrophysique du Québec (CRAQ), Université de Montréal, Département de Physique, C.P. 6128 Succ. Centre-ville, Montréal, QC, H3C 3J7, Canada*

⁴*Lincoln Laboratory, Massachusetts Institute of Technology, 244 Wood St., Lexington, MA 02420-9108, USA*

⁵*Korea Astronomy & Space Science Institute, 776 Daedeokdae-ro, Yuseong-gu, Daejeon, Republic of Korea*

⁶*University of Science and Technology, Korea, 217 Gajeong-ro, Yuseong-gu, Daejeon 34113, Republic of Korea*

(Received April 27, 2020; Revised August 5, 2020; Accepted January 26, 2022)

Submitted to ApJ

ABSTRACT

We present observations of linear polarization from dust thermal emission at 850 μm towards the starless cloud L183. These data were obtained at the James Clerk Maxwell Telescope (JCMT) using the Submillimetre Common-User Bolometer Array 2 (SCUBA-2) camera in conjunction with its polarimeter POL-2. Polarized dust emission traces the plane-of-sky magnetic field structure in the cloud, thus allowing us to investigate the role of magnetic fields in the formation and evolution of its starless core. To interpret these measurements, we first calculate the dust temperature and column density in L183 by fitting the spectral energy distribution obtained by combining data from the JCMT and the *Herschel* space observatory. We used the Davis-Chandrasekhar-Fermi technique to measure the magnetic field strength in five sub-regions of the cloud, and we find values ranging from $\sim 120 \pm 18 \mu\text{G}$ to $\sim 270 \pm 64 \mu\text{G}$ in agreement with previous studies. Combined with an average hydrogen column density (N_{H_2}) of $\sim 1.5 \times 10^{22} \text{ cm}^{-2}$ in the cloud, we also find that all five sub-regions are magnetically subcritical. These results indicate that the magnetic field in L183 is sufficiently strong to oppose the gravitational collapse of the cloud.

Keywords: ISM: Clouds, Starlight polarization, Magnetic fields

1. INTRODUCTION

In the current paradigm of star formation, the filamentary structures found in molecular clouds are expected to fragment into dense cores of dust and gas (with hydrogen volume densities of $n_{\text{H}_2} > 10^4 \text{ cm}^{-3}$) as a necessary step before stars can be formed through gravitational collapse. Indeed, far-infrared and submillimeter observations in the past two decades have shown that these dense cores are ubiquitous in nearby star-forming regions (e.g., André et al. 2014). However, not all cores are observed to harbor a protostar (e.g., di Francesco

et al. 2007). These “starless” cores are typically divided into two categories: (1) unbound cores supported against gravity by thermal pressure, which, along with gravitationally bound cores (such as B86 Alves et al. 2001), can be modeled as Bonnor-Ebert spheres (Ebert 1955; Bonnor 1956), and (2) collapsing prestellar cores transitioning into first hydrostatic cores¹ (e.g., Machida et al. 2008).

The L183 cloud (Lynds 1962, aka L134N), and its starless cores (*Spitzer* image shown in Figure 1), is an ideal candidate to study the role of magnetic fields at the on-

Corresponding author: Janik Karoly, Archana Soam
jkaroly@alumni.scu.edu, asoam@usra.edu

¹ These objects represent an early phase in the low-mass star formation process, after collapse of the parent core has begun but before a true protostar has formed.

set of star formation, and specifically to probe if they can moderate the gravitational collapse of pre-stellar cores. Indeed, at a distance of 110 pc (Franco 1989), the proximity and low Galactic longitude ($l = 6.1$) of L183 means it is a cloud with a significant number of background stars despite its high Galactic latitude ($b = 36.8$) (Pagani et al. 2003).

Lee et al. (1999, 2001, 2004) listed L183 as a possible infall candidate based on spectroscopic measurements of the CS (2–1), CS (3–2), N₂H⁺ (1–0), and DCO⁺ (2–1) molecular lines. The L183 core has a C¹⁸O depletion level typically associated with chemically-evolved cores (Tafalla 2005a,b), yet it shows no signs of hosting embedded young stellar objects even though less-evolved cores like L1521F are already undergoing star formation (Tafalla 2005a,b; Soam et al. in prep.). It is therefore possible that the gravitational collapse of L183 is significantly curtailed either because of the gas kinematics or the magnetic energy inside the core.

In this work, we investigate the contribution of the magnetic field to the stability of L183. This is achieved by using 850 μm observations obtained with the POL-2 polarimeter at the James Clerk Maxwell Telescope (JCMT). The structure of magnetic fields in the interstellar medium can be directly inferred from the polarization of dust thermal emission at far-infrared and submillimeter wavelengths (see Andersson et al. 2015, and references therein). Such emission polarization is expected to be perpendicular to the plane-of-the-sky field orientation due to the alignment of interstellar dust grains with magnetic fields through Radiative Alignment Torques (RATs). The alignment efficiency of dust grains in the dense environment of L183 will be investigated in a forthcoming paper (Andersson & Soam et al. in prep.).

Assuming a distance of 110 pc, our 850 μm observations achieve a spatial resolution of 7.5 mpc (or 1600 au) while simultaneously mapping all of the highest extinction regions in the cores over a $\sim 12'$ -wide field (see Figure 1 and 2). Crutcher et al. (2004) also observed L183 at a comparable resolution using the SCUPOL polarimeter (the predecessor of POL-2) at the JCMT, but they were limited to a much smaller $\sim 3.5'$ -wide region with a lower sensitivity than our POL-2 data (see Section 3.7). Nevertheless, their original analysis suggested that L183 may be only weakly supercritical, i.e., the magnetic energy is at least three times smaller than, and at most equal to, the gravitational energy in the core ($E_{\text{grav}}/3 < E_{\text{mag}} < E_{\text{grav}}$). With the higher sensitivity of POL-2, we significantly improve the accuracy of this criticality measurement.

The POL-2 data presented in this work provide the deepest polarization observations to date of a starless core. Although significant improvements have been made in recent years to the sensitivity of polarimetric instruments, polarimetry at far-infrared and submillimeter wavelengths still presents unique technical challenges (see Pattle & Fissel 2019) that are compounded by the faint polarization signature of starless cores. This low polarized emission is explained by the combination of two main factors: First, the dust content of starless cores is typically colder than in active star-forming regions ($T_d \approx 7$ K for L183, Pagani et al. 2003, see also Section 3.2), thus leading to weaker dust thermal emission. Second, the polarization efficiency in starless cores is known to decrease sharply as a function of visual extinction A_V (e.g., Alves et al. 2014; Jones et al. 2015), which results in a decrease of the degree of polarization in the denser parts of the cloud. Thus, observations to date have been used mostly to study magnetic fields in all but the brightest starless cores. Prior to this work, Crutcher et al. (2004) and Ward-Thompson et al. (2000) have used SCUPOL to study the bright starless cores L183, and L1544 and L43, respectively.

This paper is structured as follows: Section 2 presents the observations and the data reduction process. Section 3 provides a discussion of the main results, such as the dust properties (§3.2), the magnetic field morphology (§3.3), the field strength (§3.4), the criticality criterion (§3.5), and the energy budget of the cloud (§3.6), as well as a comparison with previous SCUPOL results (§3.7). Finally, we summarize the findings of this paper in Section 4.

2. OBSERVATIONS AND DATA REDUCTION

The observations were conducted with SCUBA-2/POL-2 at 850 μm in February and March of 2019 (M19AP009; PI: Bastien, P.) using the polarimetric daisy-map mode of the JCMT (Holland et al. 2013; Friberg et al. 2016; P. Bastien et al. in prep.). The POL-2 polarimeter, which consists of a fixed polarizer and a half-wave plate rotating at a frequency of 2 Hz, is placed in the optical path of the SCUBA-2 camera. Figure 2 shows the locations of the observations on L183 *Herschel*/SPIRE image. The weather conditions during observations were split between $\tau_{225} < 0.05$ and $0.05 < \tau_{225} < 0.08$, where τ_{225} is the atmospheric opacity at 225 GHz. The total integration time for a single field was ~ 4 hours to complete six full daisy patterns. SCUBA-2/POL-2 simultaneously collects data at 450 μm and 850 μm with effective full-width half-maximum (FWHM) beam sizes of $9''.6$ and $14''.1$, respectively (Dempsey et al. 2013). For this work, we focused

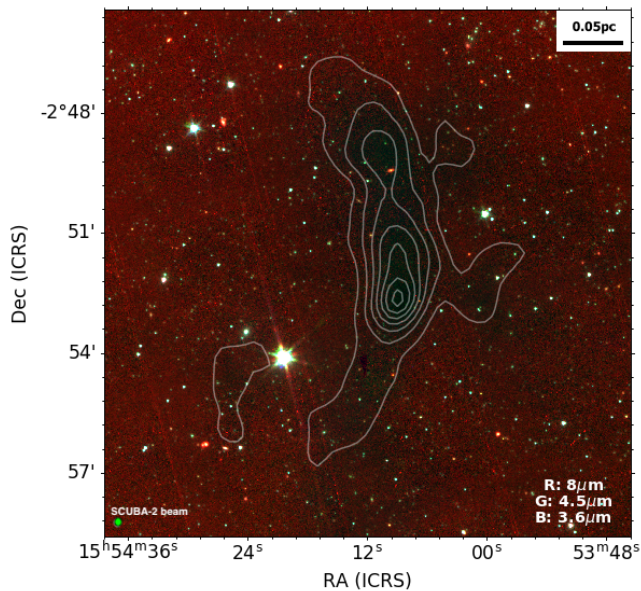


Figure 1. Combined *Spitzer* observations of L183 taken with IRAC at $8\ \mu\text{m}$, $4.5\ \mu\text{m}$, and $3.6\ \mu\text{m}$. The contours trace the $850\ \mu\text{m}$ dust emission map from SCUBA-2 starting at $10\ \text{mJy beam}^{-1}$ and increasing in increments of $20\ \text{mJy beam}^{-1}$. The green circle in the lower left corner shows the JCMT/SCUBA-2 beam size.

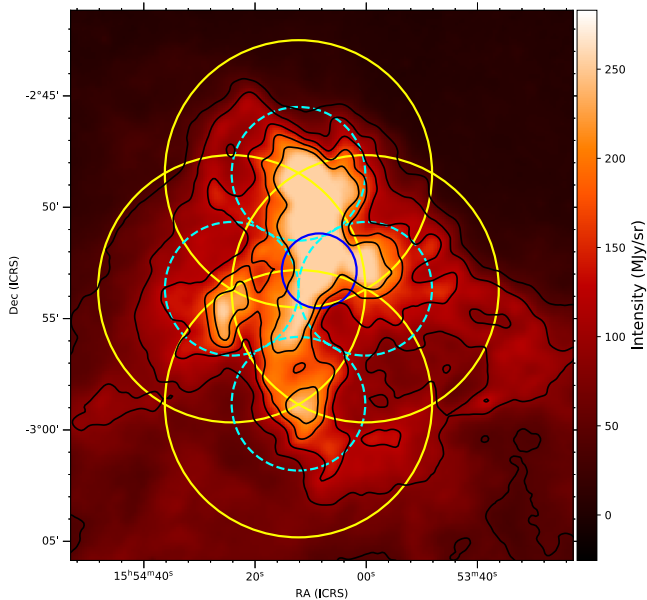


Figure 2. The dust emission toward L183 as traced by *Herschel* $500\ \mu\text{m}$ SPIRE observations. The plain blue circle in the center indicates the limited area previously observed with SCUPOL by Crutcher (2004). The yellow circles indicate the four POL-2 Daisy fields covered in our observations. These field-of-views are optimized so that their central $6'$ -wide areas (dashed cyan circles), where POL-2's sensitivity is optimal, are centered on high density regions while still fully covering the main body of the L183 cloud.

exclusively on the $850\ \mu\text{m}$ data due to the signal-to-noise ratio (SNR) in the $450\ \mu\text{m}$ data being too low to recover a sufficient number of polarization vectors for the analysis.

We observed four separate sub-regions (North, South, East, and West) overlapping near the center of the cloud. For the POL-2 daisy-map mode, a fully sampled circular region of $12'$ diameter is produced, with a high signal-to-noise coverage over the central $6'$ wide area. This observing mode is based on the SCUBA-2 constant velocity daisy scan pattern (Holland et al. 2013), but modified to have a slower scan speed (i.e., $8''\ \text{s}^{-1}$ compared to the original $155''\ \text{s}^{-1}$) to obtain sufficient on-sky data to measure the Stokes Q and U values accurately at every point of the map. The integration time decreases toward the edges of the map, which consequently leads to an increase in the root mean square (RMS) noise levels.

To reduce the data, we used the STARLINK/SMURF (Chapin et al. 2013; Currie et al. 2014) package `pol2map` specifically developed for submillimeter data obtained with the JCMT. The details of the data reduction procedure are presented in Wang et al. (2019), and we will only summarize the relevant steps here.

First, the raw bolometer time-streams are converted into Stokes I , Q , and U time-streams at a sampling rate of a full half-wave plate rotation through the process `calcqu`. A Stokes I map is then created from all Stokes I time-streams using the routine `makemap`, which is an iterative map-making process. Individual I maps corresponding to each observation were co-added to produce the initial I map of each region (cf Chapin et al. 2013). Because four separate regions were observed to cover the cloud, we co-added the initial Stokes I map from each region to get the complete Stokes I map.

The final Stokes I , Q , and U maps were obtained by running `pol2map` a second time. The initial Stokes I mosaic map is used to generate a fixed SNR-based mask for all subsequent iterations of `makemap`. During the final process, we corrected for the loss of synchronization between data values and pointing information in the data reduction process via the `skyloop2` parameter in `pol2map`. This parameter improves the recovery of fainter, extended emission in the map by iterating individual observations in parallel. This is in contrast to the traditional JCMT map-making method of deriving an iterative solution for each observation individually. The resulting Stokes I , Q , and U maps for the four sep-

² <http://starlink.eao.hawaii.edu/docs/sc22.pdf>

arate regions were then co-added to produce the final maps used for this study.

The resulting Stokes I , Q , and U maps were flux calibrated, in units of mJy beam^{-1} , using a Flux Calibration Factor (FCF) for $850 \mu\text{m}$ of 725 Jy pW^{-13} . The final co-added Stokes I , Q , and U maps have an RMS noise⁴ of $\sim 1.5 \text{ mJy beam}^{-1}$. Finally, the data were reduced with a $12''$ pixel size at each step.

After the final step of running `pol2map`, we obtain a polarization vector catalog produced from the co-added Stokes I , Q , and U maps. The final polarization values obtained here are debiased using the Stokes Q and U variances to remove the statistical bias in regions of low signal-to-noise ratio (SNR) (Wardle & Kronberg 1974).

The values for the debiased degree of polarization P were calculated from

$$P = \frac{1}{I} \sqrt{Q^2 + U^2 - \frac{1}{2}(\delta Q^2 + \delta U^2)}, \quad (1)$$

where I , Q , and U are the Stokes parameters, and δQ , and δU are the uncertainties for Stokes Q and U (see Soam et al. (2019); Wang et al. (2019)). The uncertainty δP of the polarization degree was obtained using

$$\delta P = \sqrt{\frac{(Q^2 \delta Q^2 + U^2 \delta U^2)}{I^2(Q^2 + U^2)} + \frac{\delta I^2(Q^2 + U^2)}{I^4}}, \quad (2)$$

with δI being the uncertainty for the Stokes I total intensity.

The polarization position angles θ , increasing from north to east in the sky projection, were measured using the relation

$$\theta = \frac{1}{2} \tan^{-1} \frac{U}{Q}. \quad (3)$$

The corresponding uncertainties in θ were calculated using

$$\delta \theta = \frac{1}{2} \frac{\sqrt{Q^2 \delta U^2 + U^2 \delta Q^2}}{(Q^2 + U^2)} \times \frac{180^\circ}{\pi}. \quad (4)$$

The plane-of-sky orientation of the magnetic field is inferred by rotating the polarization angles by 90° (assuming that the polarization is caused by elongated dust grains aligned perpendicular to the magnetic field).

3. ANALYSIS

3.1. Polarization and Magnetic fields

In our analysis of the POL-2 data, we only use data points where the observed uncertainties in position angle are less than 20° . Additionally, we impose an additional constraint of $I/\delta I > 10$ to improve the reliability of our analysis. We checked the quality of the data used for the analysis by examining different SNR values derived from the polarization intensity (PI) and its uncertainty (δ_{PI}). In Figure 3a, the magnetic field orientations inferred from $\text{SNR} > 3$ ($PI/\delta_{PI} > 3$; 124 blue vectors) and $\text{SNR} > 2$ ($PI/\delta_{PI} > 2$; 236 red vectors [some of the red vectors are hidden under the blue ones]) are generally consistent within the cloud. The goal of this comparison is to evaluate the validity of using the lower SNR threshold of $\text{SNR} > 2$ instead of the stricter $\text{SNR} > 3$. The additional vectors plotted using $\text{SNR} > 2$ have similar polarization percentages and position angles to the $\text{SNR} > 3$ vectors in their vicinity, which suggests that the larger population of $\text{SNR} > 2$ vectors can be used for the analysis. Additionally, in panels (b) and (c) of Figure 3, the distributions of position angles and polarization percentages follow similar behaviors, further justifying our use of the $PI/\delta_{PI} > 2$ values.

Figure 4 shows the morphology of the magnetic field in the inner parts of the L183 cloud. Here, the lengths of the vectors have been normalized for clarity; they do not represent the polarization percentage. Rather than evaluating the magnetic field structure of L183 by using a single structure function, we instead chose to split the cloud into five regions with distinct populations of magnetic field lines based on their apparent uniformity in polarization angle (see Figure 5). This allows us to employ the classical interpretation of the Davis-Chandrasekhar-Fermi method (DCF; Chandrasekhar & Fermi 1953) to derive the magnetic field strength independently for each region. Previous studies of magnetic field strength (e.g. Coudé et al. 2019), use an improved DCF method developed by Houde et al. (2009) and Hildebrand et al. (2009) which uses an angular dispersion function. We used this angular dispersion function on the five regions seen in Figure 5. However, for regions 1 through 4, the function failed to converge in 200 iterations. In region 5, the calculated turbulent-to-ordered magnetic energy ratio, $\langle B_t^2 \rangle / \langle B_o^2 \rangle$, was 21.93 ± 46.56 and the reduced chi-squared value for the fit of the angular dispersion function was 5.3. The large energy ratio uncertainty gives an indeterminate result. For these observations, the data sets are too noisy and therefore the contribution from turbulence cannot be distinguished from beam smoothing. As a reference, our noise level ($\sim 1.5 \text{ mJy beam}^{-1}$)

³ This conversion was done using the CALIBRATE-SCUBA2-DATA recipe under the PICARD package in STARLINK

⁴ This value was measured using the SCUBA2-MAPSTATS recipe under the PICARD package in STARLINK

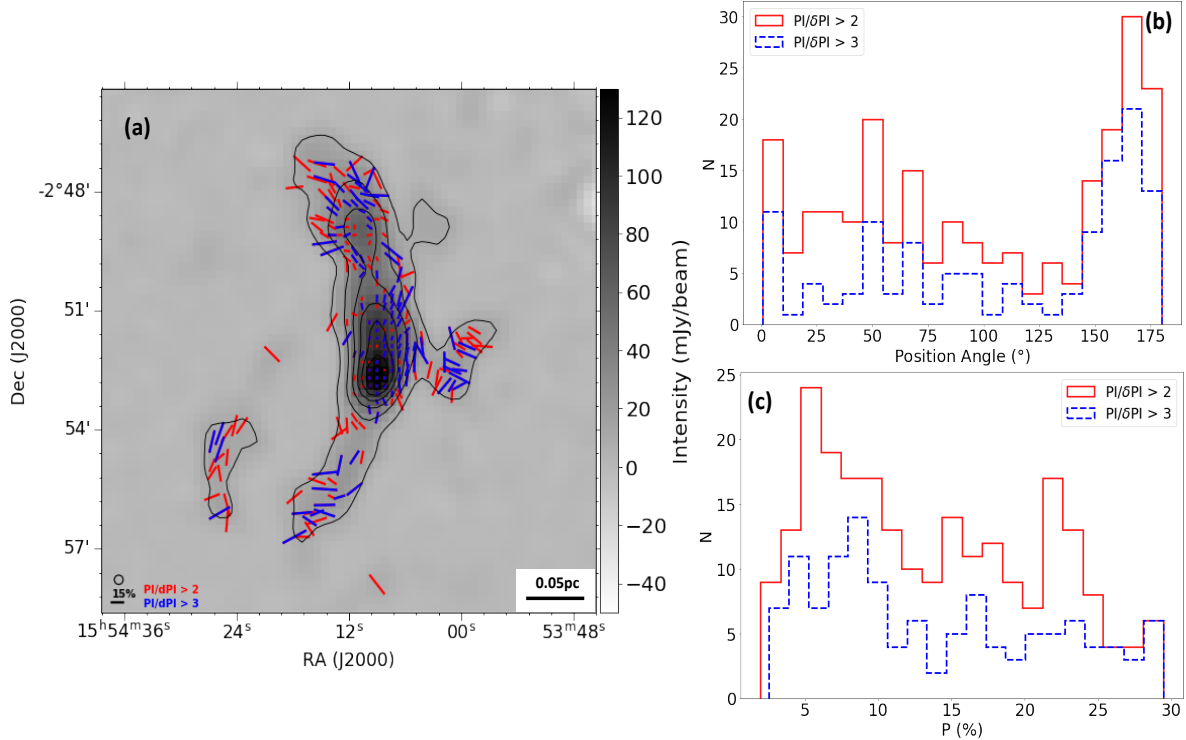


Figure 3. Panel (a) shows the magnetic field orientations in L183 with $PI/\delta PI > 2$ (red vectors) and $PI/\delta PI > 3$ (blue vectors). The vectors are plotted on the $850\ \mu\text{m}$ dust emission map with overlaid contours starting at $10\ \text{mJy beam}^{-1}$ and increasing by $20\ \text{mJy beam}^{-1}$. The JCMT $850\ \mu\text{m}$ beam size and the vector scale are shown in the bottom left corner. Panels (b) and (c) show the distributions of magnetic field position angles and polarization percentages, respectively.

is comparable to that of SCUBA-2/POL-2 observations of B1 (Coudé et al. 2019) although L183 is approximately 3 times dimmer. We therefore use the DCF method used in Crutcher et al. (2004) to calculate the magnetic field strength.

Figure 5 shows the five regions and their respective distributions of position angles, including the Gaussian fit for each. The total distribution of position angles shown in Figure 6 appears to follow a double Gaussian distribution, although the second peak is rather broad. In regions 1, 3, and 4, we have taken advantage of the 180° ambiguity in magnetic field direction (e.g., a vector with position angle of 15° shows the same direction as one with a position angle of 195°) to best demonstrate the Gaussian distributions of the position angles.

The DCF method assumes that the geometry of the magnetic field is uniform in each region, and so measuring the dispersion of position angles allows us to estimate the field strength. This dispersion in position angles is explained by local turbulence disrupting the magnetic field structure. We also assume that the distribution of vectors around the mean field direction is approximately Gaussian, and is therefore well-characterized by its stan-

dard deviation. The DCF method determines the field strength using following equation:

$$B_{pos} = Q_c \sqrt{4\pi\rho} \frac{\sigma_v}{\sigma_\theta}, \quad (5)$$

where Q_c is a correction factor that accounts for variations of the magnetic field on scales smaller than the beam, ρ is the gas density, σ_v is the one-dimensional non-thermal velocity dispersion of the gas, and σ_θ is the dispersion in polarization angle. Crutcher (2004) further approximated this formulation as

$$B_{pos} \approx 9.3 \sqrt{n(H_2)} \frac{\Delta v}{\sigma_\theta} \mu\text{G}, \quad (6)$$

where Q_c has been taken to be 0.5 (Ostriker et al. 2001), $n(H_2)$ is volume density of molecular hydrogen, and Δv is the FWHM of the gas velocity calculated by $\Delta v = \sigma_v \sqrt{8 \ln 2}$. The units are cm^{-3} for the volume density $n(H_2)$, km s^{-1} for Δv , and degrees for σ_θ .

3.2. Dust column densities and temperatures

L183 was previously observed by the *Herschel* space observatory with the Spectral and Photometric Imaging Receiver (SPIRE) at 250, 350, and $500\ \mu\text{m}$, as well as with the Photodetector Array Camera & Spectrograph

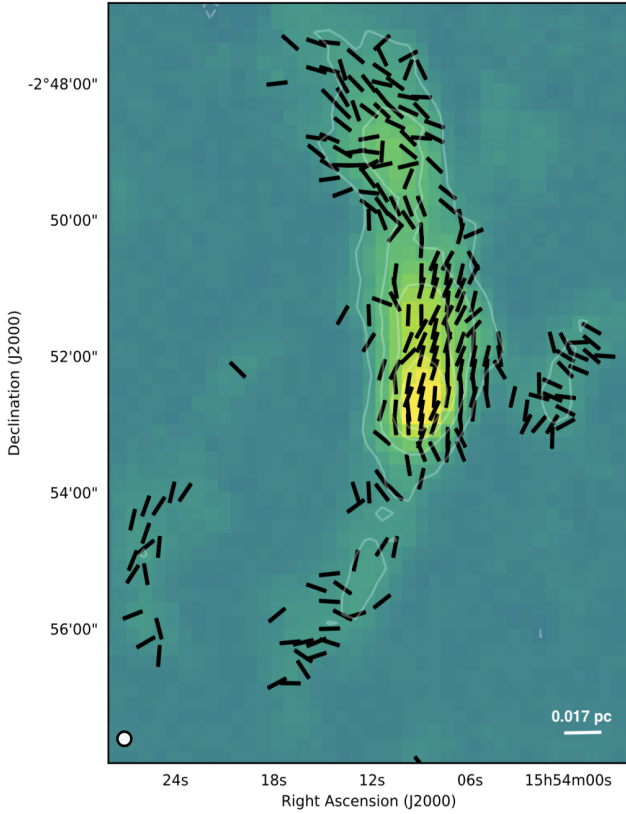


Figure 4. Magnetic field orientations in L183 obtained after rotating the polarization vectors by 90° and shown as normalized line-segments independent of the polarization degree P . These vectors correspond to data with $PI/\delta_{PI} > 2$, where PI and δ_{PI} are respectively the polarized intensity and its uncertainty. The JCMT beam size at $850 \mu\text{m}$ is shown in the lower left corner.

(PACS) at 100 and $160 \mu\text{m}$. We use this archival *Herschel* data at 160, 250, 350, and $500 \mu\text{m}$, combined with our JCMT data at $850 \mu\text{m}$, to fit a modified black-body function (see Equation 7) for the dust emission in L183. The *Herschel*/PACS, *Herschel*/SPIRE, and JCMT $850 \mu\text{m}$ images were smoothed to the SPIRE $500 \mu\text{m}$ FWHM beam size of $35''.2$ and then re-projected on a common grid.

The spectral energy distribution (SED) for each pixel was fitted assuming the following formula for a modified black-body emission (see Kauffmann et al. 2008):

$$S_\nu = B_\nu(T_d)(1 - e^{-\tau_\nu}), \quad (7)$$

$$B_\nu(T_d) = \frac{2h\nu^3}{c^2} \frac{1}{e^{h\nu/k_B T_d} - 1}, \quad (8)$$

$$\tau_\nu = \mu_{\text{H}_2} m_{\text{H}} \kappa_\nu N_{\text{H}_2}, \quad (9)$$

and

$$\kappa_\nu = \kappa_o \left(\frac{\nu}{\nu_o} \right)^\beta, \quad (10)$$

where S_ν is the measured flux at the observed frequency ν , $B_\nu(T_d)$ is the Planck function for a dust temperature T_d , τ_ν is the optical depth, μ_{H_2} is the mean molecular weight of the hydrogen gas in the cloud, m_{H} is the mass of an hydrogen atom, N_{H_2} is the column density, and κ_ν is the dust opacity (absorption coefficient). We use a value of 2.8 for μ_{H_2} , and κ_ν was calculated for each frequency observed using Equation 10, where β is the emissivity spectral index of the dust, and we assume $\kappa_o = 0.1 \text{ cm}^2 \text{ g}^{-1}$ and $\nu_o = 10^{12} \text{ Hz}$ (Beckwith et al. 1990).

The SED fitting for each pixel was completed in two steps. In the first step, β was left as a free parameter to be fitted simultaneously with the temperature T_d and the column density N_{H_2} . In the second step, we instead fixed β to the best-fit value obtained from the first step, before re-doing the SED fit to obtain the final values for the temperature and column density. The temperature and column density maps obtained through this procedure for L183 are shown in Figure 7.

The dust temperatures (left panel of Figure 7) in the filament vary approximately between 8.8 and 11 K, with very cold dust present in the two central cores of L183. These results are consistent with those of Ward-Thompson et al. (2002), who found a temperature of $10 \pm 3 \text{ K}$ in the main, southern, core by fitting a modified black-body curve to ISOPHOT measurements, as well as with those from Lehtinen et al. (2003), who found a colour temperature of $8.3 \pm 0.4 \text{ K}$.

The derived column densities (right panel of Figure 7) peak at $\sim 4 \times 10^{22} \text{ cm}^{-2}$ in the main core. The average column density in this core is around $3.0 \times 10^{22} \text{ cm}^{-2}$, which agrees with the average value of $2.7 \times 10^{22} \text{ cm}^{-2}$ found by Crutcher et al. (2004).

We estimated the hydrogen volume densities $n(\text{H}_2)$ of the five regions identified in Figure 5 by assuming they each have a cylindrical geometry, and by adopting the same procedure as Liu et al. (2018). The projected lengths L and radii r of the cylinders for each region of L183, as well as their estimated volume densities and total masses, are given in Table 1.

3.3. Magnetic field morphology

Significant amounts of complimentary optical and near-infrared (NIR) polarization data exist for L183 (Clemens 2012, Andersson et al., in prep.). Panel (a) of Figure 8 shows the optical polarization vectors overlaid on a $100 \mu\text{m}$ IRAS map. Panel (b) shows the zoomed-in area of panel (a) with the NIR and submillimeter po-

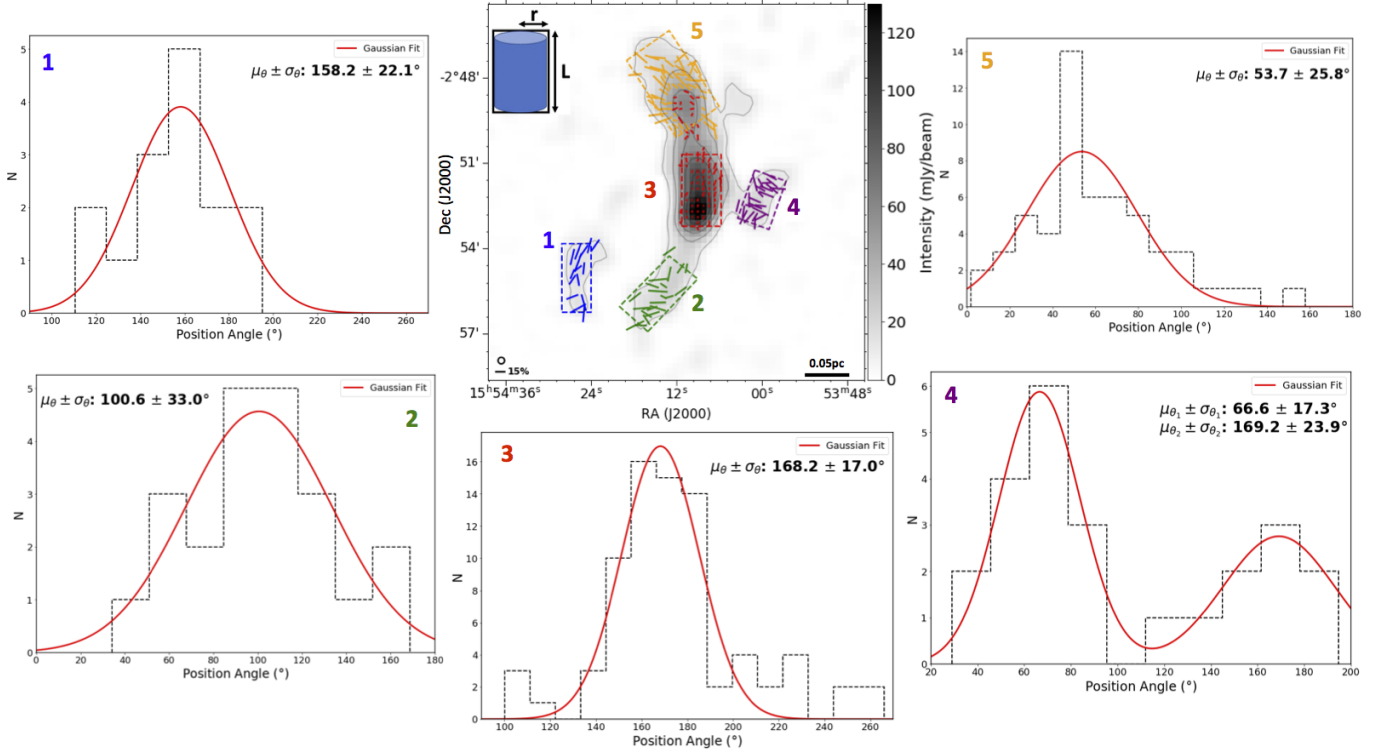


Figure 5. The five regions identified in L183 with their respective distributions of position angles. Each panel includes the mean and standard deviation of the Gaussian fit (red line). The background image is the $850\mu\text{m}$ dust emission map. The scale for the vectors is shown in the bottom left along with JCMT $850\mu\text{m}$ beam size. The red vectors show data with $I > 50\text{mJy beam}^{-1}$, while all other vectors instead show data where $I < 50\text{mJy beam}^{-1}$. The regions are drawn as rectangular boxes with dimensions listed in Table 1 as shown by the the dust emission map.

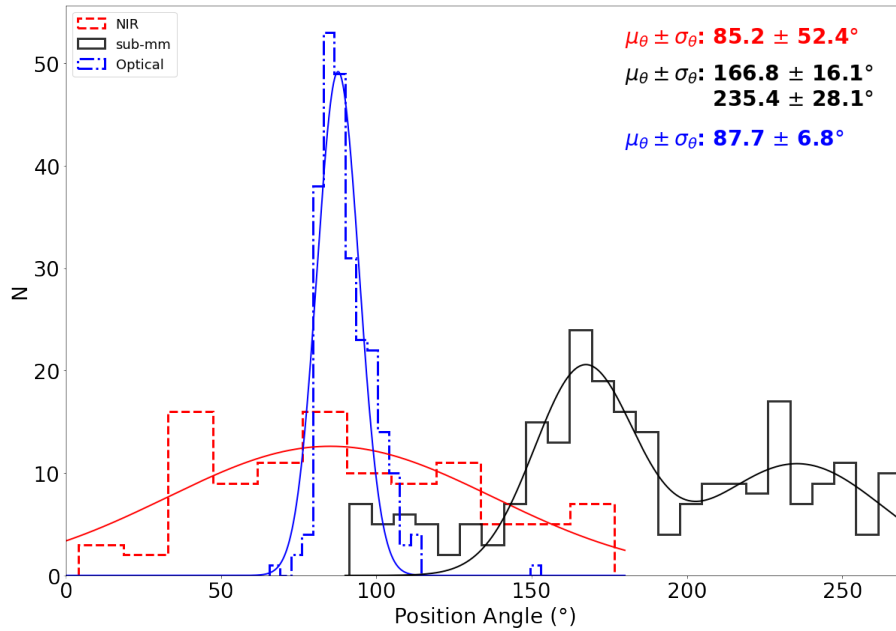


Figure 6. Histogram showing the distributions of magnetic field position angles (POL-2 polarization position angles rotated by 90°). Due to the 180° ambiguity in magnetic field direction, the POL-2 position angles that are less than 90° have been rotated by 180° to best demonstrate the observed double-Gaussian distribution. The POL-2 position angles correspond to data with $PI/\delta PI > 2$.

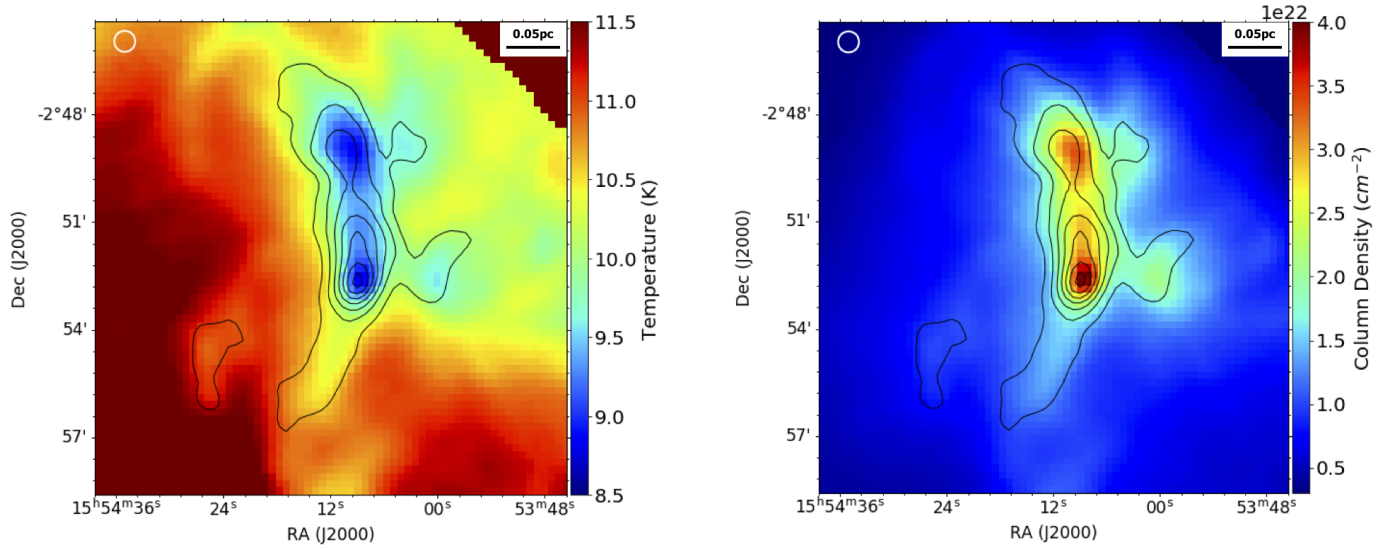


Figure 7. The left panel shows the fitted dust temperature T_d map in L183, and the right panel shows the corresponding column density N_{H_2} map. The overlaid contours on both plots are from the SCUBA-2 $850\mu\text{m}$ dust emission map. Each map is smoothed to the $35''.2$ beam size of the *Herschel* $500\mu\text{m}$ observations, which is shown by the circle in the upper left corner.

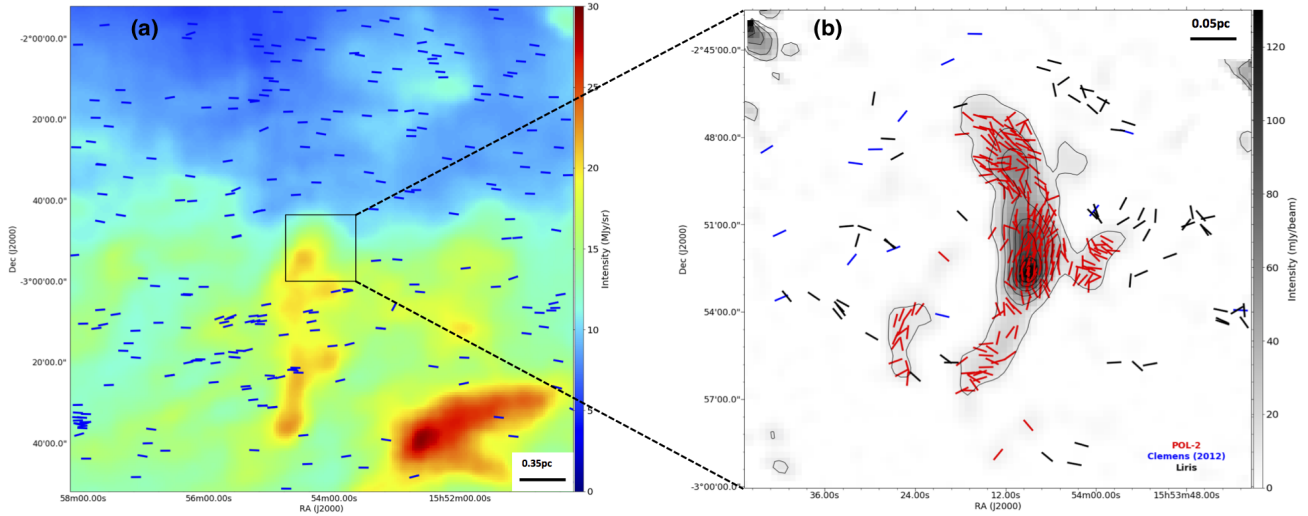


Figure 8. Panel (a): R-band polarization vectors acquired with the 2.1 m telescope at McDonald observatory (Andersson & Soam et al., in prep.) plotted on the $100\mu\text{m}$ IRAS emission map. The vector lengths are normalized and do not reflect polarization percentages. The distance scale for the image is shown in the lower right corner. The inset is the location of the L183 cloud observed at $850\mu\text{m}$ by SCUBA-2/POL-2 at the JCMT, and the zoomed-in image is shown in panel (b). Panel (b): H-band polarization measurements from LIRIS at the William Herschel Telescope (Andersson & Soam et al., in prep.) are shown in black, while H-band polarimetric data from the Mimir instrument at the Perkins telescope (Clemens 2012) are shown in blue. The $850\mu\text{m}$ polarization observations (this work) are shown with normalized red vectors that have been rotated to show the orientation of the magnetic field, consistent with the optical and NIR vectors. The contours follow the $850\mu\text{m}$ dust emission. The emissions at $100\mu\text{m}$ and $850\mu\text{m}$ microns do not peak at the same location.

larization vectors overlaid on the JCMT 850 μm dust emission map. Figure 6 shows the distribution of polarization position angles for all of the data sets, optical, NIR, and submillimeter. Because of the 180° ambiguity in polarization position angles we have, for the submillimeter polarization, added 180° to any angle less than 90° in order to make the position angle distribution continuous. Hence, the range in submillimeter wave polarization position angles is 90° to 270° .

The optical and NIR polarization data both show single peak distributions averaging around 90° , meaning that the large-scale magnetic field is oriented in the east-west direction (Figure 8). However, the polarization within the core is very different from the large-scale orientation, with a double-peaked distribution instead. We find a distinct peak for the submillimeter position angles around 180° with an additional broad distribution centered around 230° . As seen in Figure 8, the former corresponds with the magnetic field in the main core, and is perpendicular to the large-scale field. The broader distribution has a mean of 235° (or 55°) which still differs from the large-scale orientation. Neha et al. (2018) also reported the east-west orientation of B-fields in L183 using V-band polarization measurements.

Planck all-sky polarization measurements found interstellar magnetic fields mostly parallel to the diffused low-density regions of the filamentary molecular clouds, whereas field lines tend to be perpendicular in high-density regions (Planck Collaboration et al. 2015, 2016). Several studies on elongated infrared dark clouds (IRDCs) have also seen similar features. For instance, Soam et al. (2019) and Liu et al. (2018) have seen changing magnetic fields orientations from the diffuse to dense regions of the G34.43+0.24 and G035.39-00.33 clouds, respectively. It is hard to see a clear change in the magnetic field orientation within the filament containing L183, but it can be noticed that magnetic field lines are following the shape of the filament in diffuse parts such as in regions 1 and 5 (see Figure 5), but not completely parallel to the long axis of filamentary part in region 2. Whereas, in the dense core (region 3), the magnetic field lines are not perpendicular to the filament either but are instead parallel to it.

3.4. Magnetic field strength

The magnetic field strength in each of the regions identified in L183 (see Figure 5) can be calculated with Equation 6. As described in Section 3.2, the volume density for each region can be found in Table 1. Additionally, the values for Δv were taken from $\text{N}_2\text{H}^+(1-0)$ measurements by Lee et al. (2001). Furthermore, we employed a similar method to the one presented by

Crutcher et al. (2004) in order to calculate the dispersion of polarization angles σ_θ .

Within each region, we measure the difference between the polarization angle at a given position and the mean polarization angle in the region (i.e., $\theta - \bar{\theta}$), which should probe the random variations of the magnetic field. The distribution of these measured deviations was fitted with a Gaussian function, and we combined the mean of this distribution ($\Delta\theta$) and the angle uncertainties $\delta\theta$ derived from Equation 4 to calculate the dispersion σ_θ using the following relation: $\sigma_\theta = \sqrt{\delta\theta^2 - \Delta\theta^2}$.

In region 4, there appears to be two distinct populations of vectors (see corresponding histogram in Figure 5), so we found the dispersion σ_θ for both populations by splitting them between values lesser than and greater than 100° . We then took the average dispersion for both populations to calculate the magnetic field strength in that specific region.

Using the previously derived values for $n(\text{H}_2)$, Δv , and σ_θ summarized in Table 1, we calculated the magnetic field strength in each region using Equation 6. The uncertainties in B_{pos} were calculated using:

$$\frac{\delta B_{pos}}{B_{pos}} = \sqrt{\left(\frac{1}{2} \frac{\delta n(\text{H}_2)}{n(\text{H}_2)}\right)^2 + \left(\frac{\delta \Delta v}{\Delta v}\right)^2}, \quad (11)$$

where $\delta n(\text{H}_2)$ and $\delta \Delta v$ are the uncertainties in volume density and line width, respectively. We calculated the uncertainties in volume density by propagating the uncertainties for the column density. We find magnetic field strengths ranging from $\approx 120 \mu\text{G}$ to $\approx 270 \mu\text{G}$, with fractional uncertainties $\delta B_{pos}/B_{pos}$ ranging from $\approx 15\%$ to $\approx 24\%$.

3.5. Magnetic criticality of the core

The mass-to-flux ratio λ is a unit-less parameter that can be used to quantify the importance of magnetic fields relative to gravity (Crutcher 2004). This parameter can be calculated using the following relation:

$$\lambda = 7.6 \times 10^{-21} \frac{N_{\text{H}_2}}{B_{pos}}, \quad (12)$$

where N_{H_2} is the molecular hydrogen column density in cm^{-2} and B_{pos} is the plane-of-sky amplitude of the magnetic field strength in μG . When $\lambda < 1$, then the magnetic field is strong enough to restrain the gravitational collapse of the cloud; this is referred as a ‘‘magnetically sub-critical’’ regime. Alternatively, if $\lambda > 1$, then the magnetic field is insufficient by itself to oppose gravity, and the cloud is instead in a ‘‘magnetically super-critical’’ state.

Using our previously derived values for B_{pos} and N_{H_2} (see Table 1), we calculate the mass-to-flux ratios λ_{obs}

Table 1. Physical parameters for each of the five regions in L183 (see Figure 5).

Reg	r pc	L pc	$\frac{L}{r^2}$	$f(\frac{L}{r})$	N_{H_2} 10^{22} cm^{-2}	n_{H_2} 10^5 cm^{-3}	Δv km s^{-1}	M M_\odot	σ_θ $^\circ$	B_{pos} μG	λ_{cor}^a	J	$ E_{grav} $ 10^{34} J	E_{th} 10^{34} J	E_{mag} 10^{35} J	E_{kin} 10^{35} J	$\frac{E_{mag}}{E_{kin}}$	J_{tot}
1	0.016	0.081	2.53	1.15876	0.9 ± 0.2	1.2 ± 0.3	0.24 ± 0.03	0.5 ± 0.1	3.7	206 ± 33	0.11 ± 0.03	2.97	7.42 ± 2.97	2.50 ± 0.50	3.2 ± 1.0	1.1 ± 0.5	2.8 ± 0.9	0.17
2	0.021	0.077	1.83	0.98055	1.2 ± 0.3	1.2 ± 0.3	0.35 ± 0.03	0.9 ± 0.2	9.1	123 ± 18	0.25 ± 0.07	4.40	18.3 ± 8.1	4.16 ± 0.92	1.9 ± 0.6	3.6 ± 1.3	0.5 ± 0.2	0.34
3	0.022	0.080	1.82	0.97653	2.8 ± 1.3	2.6 ± 1.2	0.28 ± 0.01	2.2 ± 1.0	4.9	272 ± 64	0.26 ± 0.14	10.70	113 ± 103	10.6 ± 4.8	10.5 ± 5.0	6.2 ± 4.3	1.7 ± 0.8	0.68
4	0.019	0.058	1.53	0.89089	1.8 ± 0.6	2.0 ± 0.6	0.21 ± 0.01	0.9 ± 0.3	6.0	144 ± 24	0.31 ± 0.12	5.42	23.1 ± 15.4	4.25 ± 1.42	1.6 ± 0.5	1.6 ± 0.7	1.0 ± 0.3	0.73
5	0.029	0.102	1.76	0.96039	1.9 ± 0.8	1.3 ± 0.6	0.26 ± 0.01	2.5 ± 1.0	6.6	135 ± 28	0.36 ± 0.17	9.42	113 ± 90	12.0 ± 4.8	5.7 ± 2.4	6.3 ± 3.5	0.9 ± 0.3	0.95

a. λ_{cor} is the corrected mass-to-flux ratio.

for each region in L183. We note, however, that these ratios can be overestimated due to geometric biases. For this reason, we followed the same procedure as Crutcher (2004), and divided our values of λ_{obs} by 3 to obtain the corrected mass-to-flux ratios λ_{cor} provided in Table 1. These results indicate that the L183 cloud as a whole is magnetically sub-critical.

Based on their survey of molecular lines in starless cores, Lee & Myers (2011) initially found L183 to be a potentially contracting core. However, according to their results (see Figure 10 of Lee & Myers (2011)), L183 could also be identified as an oscillating core if the classification criteria are slightly relaxed. Our findings that L183 is magnetically sub-critical may therefore help to clarify the dynamical state of this cloud, which was previously unclear using only molecular line data. However, such an expanded analysis would be beyond the scope of this paper.

3.6. Energy budget of the cloud

The energy budget of a cloud can be estimated by calculating and comparing its thermal E_{th} , kinematic E_{kin} , magnetic E_{mag} , and gravitational E_{grav} energies. First, we define the following relations:

$$E_{mag} = \frac{B^2 V}{2\mu_o}, \quad (13)$$

$$E_{th} = \frac{3M\Delta v_{th}^2}{2}, \quad (14)$$

$$E_{kin} = \frac{3M\Delta v^2}{2}, \quad (15)$$

$$\Delta v = \sqrt{(\Delta v_{turb})^2 + (\Delta v_{th})^2}, \quad (16)$$

and

$$(\Delta v_{th})^2 = v_{sound}^2 = \frac{k_B T_{gas}}{\mu_{free} m_H}, \quad (17)$$

where V is the volume, μ_o is the permeability of free space, μ_{free} is the mean molecular weight of free particles, Δv is the total FWHM line width from Equation 16, and Δv_{th} and Δv_{turb} are respectively the contributions of the thermal and turbulent components of this line width. Note that the kinematic energy E_{kin} combines the contribution due to thermal motion of gas particles, as well as the usually stronger energy due to non-thermal supersonic motions from turbulence. The mass M for the region is calculated with $M = n(H_2)m_H\mu_{H_2}\pi r^2 L$.

In the previous relations, we assume a mean molecular weight $\mu_{free} = 2.37$ for a gas mixture of H ($X = 0.71$), He ($Y = 0.27$), and metals ($Z = 0.02$), but are neglecting

the contribution of metals. Furthermore, we adopt the turbulent line widths Δv_{turb} from Lee et al. (2001), and the thermal component Δv_{th} was calculated using the measured excitation temperature of 4.6 K from Pagani et al. (2005).

To find out if the five regions we identified in the L183 cloud are gravitationally bound, we also need to compute their gravitational energies. There is no analytical solution for the gravitational potential of finite uniform cylindrical clouds (Kellogg 1929). Nevertheless, a numerical solution can be expressed as a function $f(L/D)$ of the ratio between the length L and the diameter D of the cylinder (Bastien & Mitalas 1979). The values of this function have been tabulated by Bastien (1983) for typical values of L/D from 0.2 to 10.0. If we define a Jeans number, J , one can show that

$$J_{cyl} = \frac{|E_{grav}|}{E_{th}} = \frac{G m}{\frac{k_B T}{\mu_{free} m_H}} f\left(\frac{L}{D}\right), \quad (18)$$

$$J_{cyl} = 3 \frac{m}{m_c} f\left(\frac{L}{D}\right), \quad (19)$$

where $m = M/L$ is the linear mass of the cloud.

The critical linear mass for an infinite cylinder is given by:

$$m_c = \left(\frac{M}{L}\right)_c = \frac{3k_B T}{b G \mu_{free} m_H}. \quad (20)$$

The constant b depends on the density distribution (i.e., $b = 1$ for uniform density cylinders (McCrea 1957), and $b = 3/2$ for equilibrium cylinders (Ostriker 1964)). When $m > m_c$, the filament (cylinder) collapses along its axis. Otherwise, if $m < m_c$, the infinite cloud will not collapse, even by increasing the external pressure. The values of $f(L/D)$ for our five regions were determined by a linear interpolation of $\log[f(L/D)]$ between the known values in Table 1 from Bastien (1983). We used Equation 20 with $b = 1$ for uniform density cylinders to get $m_c = 7.5 M_\odot / pc$ assuming a temperature $T = 4.6 K$. Combining Equations 14 and 18, we obtain the gravitational energy E_{grav} of the cylinders, which can be found in Table 1. The value of E_{grav} can be found using equation below.

$$E_{grav} = -\frac{9}{4} \frac{G M^2}{b L} f(L/D) \quad (21)$$

The derived values of the Jeans numbers ($=1/\alpha$ in many other works) are all $> \approx 3.0$, and are larger than the critical Jeans numbers for cylinders with $1.5 < L/D < 2.5$ which is ≈ 0.8 (Bastien 1983). This means that all five regions are gravitationally bound if we consider only gravity and thermal pressure. Moreover, they

can accommodate other forces that tend to counter gravity, such as turbulence and magnetic fields.

To take into account other forces, we computed the following quantity:

$$J_{tot} = \frac{E_{grav}}{E_{kin} + E_{mag}}. \quad (22)$$

We see that all the regions in L183, except maybe region 5 (see Figure 5), will not be bound when thermal and non-thermal motions, in addition to magnetic fields, are taken into account. However, we have to be careful since the contribution of a magnetic field depends on its configuration. For example, a toroidal field will constrain the gas on the axis of the filament, and a poloidal field aligned with the axis will increase motions along that axis. In any case, as shown with hydrodynamics calculations, gravity produces significant motions of material along the axis of the filament. After some time, these motions increase the line mass and will make it possible to get sections of the filament to become gravitationally unstable, even if they were originally stable. However, a truly infinite cylindrical cloud will not produce motions along its axis, unless it has density perturbations along its axis.

3.7. Comparison with previous polarization measurements in L183

Matthews et al. (2009) reanalyzed the polarization data previously obtained towards L183 using SCUBA-2/POL-2's predecessor, SCUPOL (Ward-Thompson et al. 2000; Crutcher et al. 2004). They reported 26 data points with $P/\delta P > 2$ towards the main core of L183, while our observations yield 236 such data points in the whole filamentary cloud structure (including the main core). The two data sets are spatially coincident to within $\sim 6''$. In Figure 9, the comparisons between SCUPOL and POL-2 polarization percentages (upper panel) and position angles (lower panel) for L183 are plotted. The degrees of polarization in both samples agree within a 3σ range. We added 180° to the SCUBA-2/POL-2 position angles that are less than 90° to try and find a better relationship between SCUPOL and POL-2 detections. Our data achieve a higher SNR and sensitivity both in the region studied by Matthews et al. (2009) and Crutcher et al. (2004) and in the rest of the large-scale filament, and so the observed differences are likely due to the increased sensitivity of SCUBA-2/POL-2 relative to SCUPOL.

We also compared our results to the magnetic field strength estimates from the SCUPOL data by limiting our DCF analysis to only the region of L183 analyzed by Crutcher et al. (2004). Following their method,

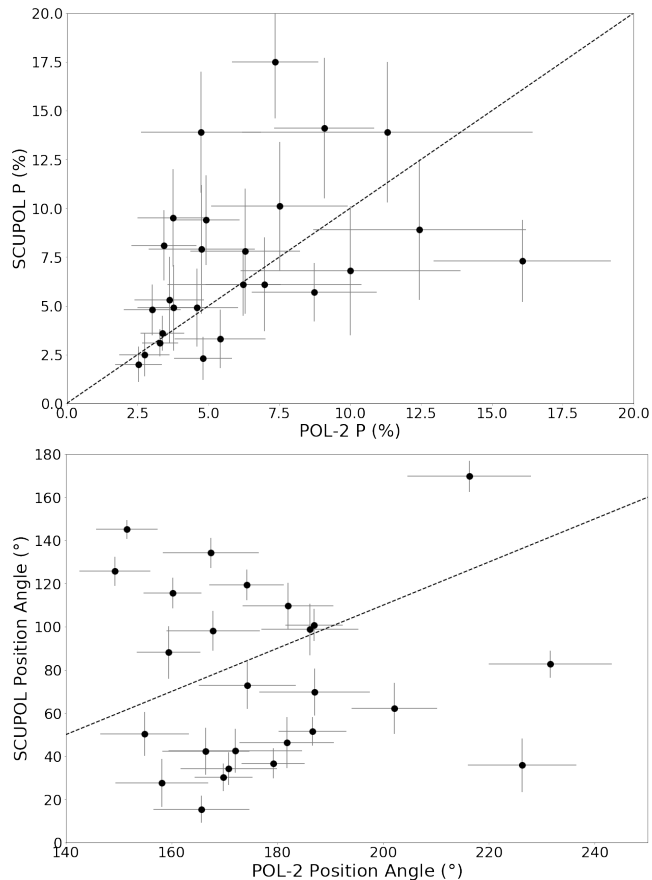


Figure 9. The upper panel shows a comparison between SCUPOL (Matthews et al. 2009) and SCUBA-2/POL-2 (this work) polarization percentages measured toward L183. Similarly, the lower panel shows a comparison of polarization angles. In both plots, the dashed line shows the corresponding one-to-one relation.

we treated the region as a sphere and used the velocity dispersion value of 0.22 km s^{-1} from Caselli et al. (2002). We obtained $B_{pos} = 105 \pm 24 \mu\text{G}$, consistent with $\sim 80 \mu\text{G}$ from Crutcher et al. (2004).

4. SUMMARY

1. We presented the deepest $850 \mu\text{m}$ continuum Stokes I , Q , and U observations to date of the starless cloud L183. The Stokes I map shows an elongated filamentary structure containing two distinct dense cores, as well as several additional, less dense condensations.
2. We compared the magnetic field morphology derived from POL-2 data to that of optical and near infrared data. We found that, while the large-scale field in the extended cloud run in an east-west direction, the magnetic fields in the cores are predominantly oriented north-south along the direction of the filament’s elongation.

3. The L183 filamentary structure separates into five sub-regions for which we performed individual analysis of the polarization degree, as well as of the orientation and strength of the magnetic field. Out of these five regions, region 3, which contains the main core of L183, is found to be the densest ($n_{H_2} = 2.6 \times 10^5 \text{ cm}^{-3}$) with the strongest magnetic field ($B = 272 \mu\text{G}$). All other relatively diffuse regions have similar density and field strengths.
4. We estimated the gas column density and the dust temperature of the mapped region by supplementing our $850 \mu\text{m}$ data with *Herschel* SPIRE/PACS continuum observations. The average values of column density and temperature in the filament are $\sim 1.5 \times 10^{22} \text{ cm}^{-2}$ and $\sim 10 \text{ K}$, respectively.
5. The magnetic field strength in each of the mapped regions ranges from $\sim 120 \pm 18 \mu\text{G}$ to $\sim 270 \pm 64 \mu\text{G}$. With our derived field strength and column density, we calculated the criticality parameter λ_{cor} in these five regions, and found values ranging from 0.1 to 0.4. These results suggest that the L183 is magnetically sub-critical everywhere, except for region 5 which could be gravitationally bound because of its lower magnetic energy and somewhat larger mass.

We thank the anonymous referee for an encouraging and constructive report, which helped in improving the final manuscript. J.K. is supported by Santa Clara University. A.S. and B-G.A. are supported by NSF Grant-1715876. This research was conducted in part at the SOFIA Science Center, which is operated by the Universities Space Research Association under contract NNA17BF53C with the National Aeronautics and Space Administration. C.W.L. is supported by the Basic Science Research Program through the National Research Foundation of Korea (NRF) funded by the Ministry of Education, Science and Technology (NRF-2019R1A2C1010851). J.E.V. acknowledges financial support from NASA through award # SOF 05-0038 issued by USRA. The JCMT is operated by the East Asian Observatory on behalf of National Astronomical Observatory of Japan; Academia Sinica Institute of Astronomy and Astrophysics; the Korea Astronomy and Space Science Institute; the Operation, Maintenance and Upgrading Fund for Astronomical Telescopes and Facility Instruments, budgeted from the Ministry of Finance of China. SCUBA-2 and POL-2 were built

through grants from the Canada Foundation for Innovation. This research used the facilities of the Canadian Astronomy Data Centre operated by the National Research Council of Canada with the support of the Canadian Space Agency.

This research made use of Astropy,⁵ a community-developed core Python package for Astronomy (Astropy

Collaboration et al. 2013; Price-Whelan et al. 2018). The Starlink software (Currie et al. 2014) is currently supported by the East Asian Observatory.

Facility: JCMT (SCUBA-2, POL-2)

Software: Starlink (Currie et al. 2014), Astropy (Astropy Collaboration et al. 2013).

REFERENCES

- Alves, F. O., Frau, P., Girart, J. M., et al. 2014, *A&A*, 569, L1, doi: [10.1051/0004-6361/201424678](https://doi.org/10.1051/0004-6361/201424678)
- Alves, J. F., Lada, C. J., & Lada, E. A. 2001, *Nature*, 409, 159
- Andersson, B. G., Lazarian, A., & Vaillancourt, J. E. 2015, *ARA&A*, 53, 501, doi: [10.1146/annurev-astro-082214-122414](https://doi.org/10.1146/annurev-astro-082214-122414)
- André, P., Di Francesco, J., Ward-Thompson, D., et al. 2014, in *Protostars and Planets VI*, ed. H. Beuther, R. S. Klessen, C. P. Dullemond, & T. Henning, 27, doi: [10.2458/azu_uapress_9780816531240-ch002](https://doi.org/10.2458/azu_uapress_9780816531240-ch002)
- Astropy Collaboration, Robitaille, T. P., Tollerud, E. J., et al. 2013, *A&A*, 558, A33, doi: [10.1051/0004-6361/201322068](https://doi.org/10.1051/0004-6361/201322068)
- Bastien, P. 1983, *A&A*, 119, 109
- Bastien, P., & Mitalas, R. 1979, *MNRAS*, 186, 755, doi: [10.1093/mnras/186.4.755](https://doi.org/10.1093/mnras/186.4.755)
- Beckwith, S. V. W., Sargent, A. I., Chini, R. S., & Guesten, R. 1990, *AJ*, 99, 924, doi: [10.1086/115385](https://doi.org/10.1086/115385)
- Bonnor, W. B. 1956, *MNRAS*, 116, 351, doi: [10.1093/mnras/116.3.351](https://doi.org/10.1093/mnras/116.3.351)
- Caselli, P., Benson, P. J., Myers, P. C., & Tafalla, M. 2002, *ApJ*, 572, 238, doi: [10.1086/340195](https://doi.org/10.1086/340195)
- Chandrasekhar, S., & Fermi, E. 1953, *ApJ*, 118, 113, doi: [10.1086/145731](https://doi.org/10.1086/145731)
- Chapin, E. L., Berry, D. S., Gibb, A. G., et al. 2013, *MNRAS*, 430, 2545, doi: [10.1093/mnras/stt052](https://doi.org/10.1093/mnras/stt052)
- Clemens, D. P. 2012, *ApJ*, 748, 18, doi: [10.1088/0004-637X/748/1/18](https://doi.org/10.1088/0004-637X/748/1/18)
- Coudé, S., Bastien, P., Houde, M., et al. 2019, *ApJ*, 877, 88, doi: [10.3847/1538-4357/ab1b23](https://doi.org/10.3847/1538-4357/ab1b23)
- Crutcher, R. M. 2004, *Ap&SS*, 292, 225, doi: [10.1023/B:ASTR.0000045021.42255.95](https://doi.org/10.1023/B:ASTR.0000045021.42255.95)
- Crutcher, R. M., Nutter, D. J., Ward-Thompson, D., & Kirk, J. M. 2004, *ApJ*, 600, 279, doi: [10.1086/379705](https://doi.org/10.1086/379705)
- Currie, M. J., Berry, D. S., Jenness, T., et al. 2014, *Astronomical Society of the Pacific Conference Series*, Vol. 485, *Starlink Software in 2013*, ed. N. Manset & P. Forshay, 391
- Dempsey, J. T., Friberg, P., Jenness, T., et al. 2013, *MNRAS*, 430, 2534, doi: [10.1093/mnras/stt090](https://doi.org/10.1093/mnras/stt090)
- di Francesco, J., Evans, N. J., I., Caselli, P., et al. 2007, in *Protostars and Planets V*, ed. B. Reipurth, D. Jewitt, & K. Keil, 17. <https://arxiv.org/abs/astro-ph/0602379>
- Ebert, R. 1955, *ZA*, 37, 217
- Franco, G. A. P. 1989, *A&A*, 223, 313
- Friberg, P., Bastien, P., Berry, D., et al. 2016, *Society of Photo-Optical Instrumentation Engineers (SPIE) Conference Series*, Vol. 9914, *POL-2: a polarimeter for the James-Clerk-Maxwell telescope*, 991403, doi: [10.1117/12.2231943](https://doi.org/10.1117/12.2231943)
- Hildebrand, R. H., Kirby, L., Dotson, J. L., Houde, M., & Vaillancourt, J. E. 2009, *The Astrophysical Journal*, 696, 567, doi: [10.1088/0004-637x/696/1/567](https://doi.org/10.1088/0004-637x/696/1/567)
- Holland, W. S., Bintley, D., Chapin, E. L., et al. 2013, *MNRAS*, 430, 2513, doi: [10.1093/mnras/sts612](https://doi.org/10.1093/mnras/sts612)
- Houde, M., Vaillancourt, J. E., Hildebrand, R. H., Chitsazzadeh, S., & Kirby, L. 2009, *The Astrophysical Journal*, 706, 1504, doi: [10.1088/0004-637x/706/2/1504](https://doi.org/10.1088/0004-637x/706/2/1504)
- Jones, T. J., Bagley, M., Krejny, M., Andersson, B. G., & Bastien, P. 2015, *AJ*, 149, 31, doi: [10.1088/0004-6256/149/1/31](https://doi.org/10.1088/0004-6256/149/1/31)
- Kauffmann, J., Bertoldi, F., Bourke, T. L., Evans, N. J., I., & Lee, C. W. 2008, *A&A*, 487, 993, doi: [10.1051/0004-6361:200809481](https://doi.org/10.1051/0004-6361:200809481)
- Lee, C. W., & Myers, P. C. 2011, *ApJ*, 734, 60, doi: [10.1088/0004-637X/734/1/60](https://doi.org/10.1088/0004-637X/734/1/60)
- Lee, C. W., Myers, P. C., & Plume, R. 2004, *ApJS*, 153, 523, doi: [10.1086/421996](https://doi.org/10.1086/421996)
- Lee, C. W., Myers, P. C., & Tafalla, M. 1999, *ApJ*, 526, 788, doi: [10.1086/308027](https://doi.org/10.1086/308027)
- . 2001, *ApJS*, 136, 703, doi: [10.1086/322534](https://doi.org/10.1086/322534)
- Lehtinen, K., Mattila, K., Lemke, D., et al. 2003, *A&A*, 398, 571, doi: [10.1051/0004-6361:20021411](https://doi.org/10.1051/0004-6361:20021411)

⁵ <http://www.astropy.org>

- Liu, T., Li, P. S., Juvella, M., et al. 2018, *ApJ*, 859, 151, doi: [10.3847/1538-4357/aac025](https://doi.org/10.3847/1538-4357/aac025)
- Lynds, B. T. 1962, *ApJS*, 7, 1.
http://adsabs.harvard.edu/cgi-bin/nph-bib_query?bibcode=1962ApJS....7....1L&db_key=AST
- Machida, M. N., Inutsuka, S.-i., & Matsumoto, T. 2008, *ApJ*, 676, 1088, doi: [10.1086/528364](https://doi.org/10.1086/528364)
- Matthews, B. C., McPhee, C. A., Fissel, L. M., & Curran, R. L. 2009, *ApJS*, 182, 143, doi: [10.1088/0067-0049/182/1/143](https://doi.org/10.1088/0067-0049/182/1/143)
- McCrea, W. H. 1957, *MNRAS*, 117, 562, doi: [10.1093/mnras/117.5.562](https://doi.org/10.1093/mnras/117.5.562)
- Neha, S., Maheswar, G., Soam, A., & Lee, C. W. 2018, *MNRAS*, 476, 4442, doi: [10.1093/mnras/sty485](https://doi.org/10.1093/mnras/sty485)
- Ostriker, E. C., Stone, J. M., & Gammie, C. F. 2001, *ApJ*, 546, 980, doi: [10.1086/318290](https://doi.org/10.1086/318290)
- Ostriker, J. 1964, *ApJ*, 140, 1529, doi: [10.1086/148057](https://doi.org/10.1086/148057)
- Pagani, L., Pardo, J. R., Apponi, A. J., Bacmann, A., & Cabrit, S. 2005, *A&A*, 429, 181, doi: [10.1051/0004-6361:20041044](https://doi.org/10.1051/0004-6361:20041044)
- Pagani, L., Lagache, G., Bacmann, A., et al. 2003, *A&A*, 406, L59, doi: [10.1051/0004-6361:20030903](https://doi.org/10.1051/0004-6361:20030903)
- Pattle, K., & Fissel, L. 2019, *Frontiers in Astronomy and Space Sciences*, 6, 15, doi: [10.3389/fspas.2019.00015](https://doi.org/10.3389/fspas.2019.00015)
- Planck Collaboration, Ade, P. A. R., Aghanim, N., et al. 2015, *A&A*, 576, A104, doi: [10.1051/0004-6361/201424082](https://doi.org/10.1051/0004-6361/201424082)
- . 2016, *A&A*, 586, A138, doi: [10.1051/0004-6361/201525896](https://doi.org/10.1051/0004-6361/201525896)
- Price-Whelan, A. M., Sipőcz, B. M., Günther, H. M., et al. 2018, *AJ*, 156, 123, doi: [10.3847/1538-3881/aabc4f](https://doi.org/10.3847/1538-3881/aabc4f)
- Soam, A., Liu, T., Andersson, B. G., et al. 2019, *ApJ*, 883, 95, doi: [10.3847/1538-4357/ab39dd](https://doi.org/10.3847/1538-4357/ab39dd)
- Tafalla, M. 2005a, in *IAU Symposium*, Vol. 231, *Astrochemistry: Recent Successes and Current Challenges*, ed. D. C. Lis, G. A. Blake, & E. Herbst, 17–26, doi: [10.1017/S1743921306007009](https://doi.org/10.1017/S1743921306007009)
- Tafalla, M. 2005b, *Astrophysics and Space Science Library*, Vol. 324, *Starless Cores*, ed. M. S. N. Kumar, M. Tafalla, & P. Caselli, 31, doi: [10.1007/0-387-26357-8_3](https://doi.org/10.1007/0-387-26357-8_3)
- Wang, J.-W., Lai, S.-P., Eswaraiah, C., et al. 2019, *ApJ*, 876, 42, doi: [10.3847/1538-4357/ab13a2](https://doi.org/10.3847/1538-4357/ab13a2)
- Ward-Thompson, D., André, P., & Kirk, J. M. 2002, *MNRAS*, 329, 257, doi: [10.1046/j.1365-8711.2002.04969.x](https://doi.org/10.1046/j.1365-8711.2002.04969.x)
- Ward-Thompson, D., Kirk, J. M., Crutcher, R. M., et al. 2000, *ApJL*, 537, L135, doi: [10.1086/312764](https://doi.org/10.1086/312764)
- Wardle, J. F. C., & Kronberg, P. P. 1974, *ApJ*, 194, 249, doi: [10.1086/153240](https://doi.org/10.1086/153240)